Aalborg Universitet

AALBORG UNIVERSITY
DENMARK

Variable-Speed PICO Hydel Energy Storage With Synchronverter Control to Emulate Virtual Inertia in Autonomous Microgrids

Vasudevan, Krishnakumar R.; Ramachandaramurthy, Vigna K.; Venugopal, Gomathi; Guerrero, Josep M.; Ekanayake, Janaka B.; Tiong, Sieh Kiong

Published in:
IEEE Systems Journal

DOI (link to publication from Publisher):
10.1109/JSYST.2021.3053358

Publication date:
2022

Document Version
Accepted author manuscript, peer reviewed version

Link to publication from Aalborg University

Citation for published version (APA):
Vasudevan, K. R., Ramachandaramurthy, V. K., Venugopal, G., Guerrero, J. M., Ekanayake, J. B., & Tiong, S. K. (2022). Variable-Speed PICO Hydel Energy Storage With Synchronverter Control to Emulate Virtual Inertia in Autonomous Microgrids. *IEEE Systems Journal*, *16*(1), 452-463. https://doi.org/10.1109/JSYST.2021.3053358

General rights
Copyright and moral rights for the publications made accessible in the public portal are retained by the authors and/or other copyright owners and it is a condition of accessing publications that users recognise and abide by the legal requirements associated with these rights.

- Users may download and print one copy of any publication from the public portal for the purpose of private study or research.
- You may not further distribute the material or use it for any profit-making activity or commercial gain
- You may freely distribute the URL identifying the publication in the public portal -

Take down policy
If you believe that this document breaches copyright please contact us at vbn@aub.aau.dk providing details, and we will remove access to the work immediately and investigate your claim.

This article has been accepted for inclusion in a future issue of this journal. Content is final as presented, with the exception of pagination.

Variable-Speed PICO Hydel Energy Storage With Synchronverter Control to Emulate Virtual Inertia in Autonomous Microgrids

Krishnakumar R. Vasudevan, *Graduate Student Member, IEEE*, Vigna K. Ramachandaramurthy, *Senior Member, IEEE*, Gomathi Venugopal, Josep M. Guerrero, *Fellow, IEEE*, Janaka B. Ekanayake, *Fellow, IEEE*, and Sieh Kiong Tiong, *Member, IEEE*

***Abstract*—Autonomous microgrids are potential alternative to grid connectivity for powering remote communities around the globe. A sustainable microgrid with renewables and energy storage having minimum operation and maintenance routines is the most sought option. Batteries are predominantly used to support the stochastic behavior of renewables in such microgrids. However, they are prone to frequent failure and require periodic maintenance, which demands an alternative. Thus, in this article, the renewable powered irrigation system in India was configured to form sustainable pico hydel energy storage (PHES). To enhance the inertia of the microgrid with static sources, virtual inertia capability was induced into PHES by modified synchronverter technology. First, the small-signal modeling approach was presented to derive the closed-loop transfer function of the system. Subsequently, the effect of control parameter variation on system stability and the interaction between the governor and the synchronverter was investigated using eigenvalue analysis. Next, the performance of synchronverter was compared with the established vector control through time-domain simulations in MATLAB/Simulink. The simulation results revealed that the proposed strategy improved the inertial response of PHES and outperformed vector control by reducing peak overshoot, settling time, and steady-state error.**

***Index Terms*—Energy storage, pumped hydro storage (PHS), rural electrification, synchronverter, virtual inertia, virtual synchronous generator.**

Manuscript received June 19, 2020; revised December 3, 2020; accepted January 14, 2021. This work was supported in part by the Long Term Research Grant Scheme, Ministry of Education Malaysia for the program titled "Decarbonisation of Grid with an Optimal Controller and Energy Management for Energy Storage System in Microgrid Applications." *(Corresponding author: Krishnakumar R. Vasudevan.)*

Krishnakumar R. Vasudevan and Vigna K. Ramachandaramurthy are with the Institute of Power Engineering, Universiti Tenaga Nasional, Kajang 43000, Malaysia (e-mail: vasudevkrishna.ceg@gmail.com; vigna@uniten.edu.my).

Gomathi Venugopal is with the Department of Electrical and Electronics Engineering, Anna University, Chennai 600025, India (e-mail: gomesceg@gmail.com).

Josep M. Guerrero is with the Department of Energy Technology, Aalborg University, Aalborg DK-9220, Denmark (e-mail: joz@et.aau.dk).

Janaka B. Ekanayake is with the Department of Electrical and Electronics Engineering, University of Peradeniya, Galaha 20400, Sri Lanka (e-mail: jbe@ee.pdn.ac.lk).

Sieh Kiong Tiong is with the Institute of Sustainable Energy, Universiti Tenaga Nasional, Kajang 43000, Malaysia (e-mail: siehkiong@uniten.edu.my).

Digital Object Identifier 10.1109/JSYST.2021.3053358

I. Introduction

ACCORDING to the Ministry of Power, Government of India, approximately 18 734 rural households are yet to be electrified at present [1]. Although the number had remarkably reduced from a whopping 24 847 762 in October 2017, the definition of rural electrification does not guarantee reliable power supply round the clock. Under such circumstances, autonomous microgrids with renewable energy sources are a promising solution to electrify these underprivileged rural communities. However, the stability of such microgrids becomes imperative due to the stochastic variation of meteorological variables. Hence, an adequate buffer of approximately 10% of the system power rating with the energy storage systems (EESs) is maintained to ensure stability [2]. Lead-acid batteries were vastly deployed in microgrids around the globe due to its low capital cost and easy accessibility [3]. However, it was reported that the high failure rate of such microgrids is due to the poor reliability of lead-acid batteries [4]. Among other ESS, pumped hydro storage (PHS) is the most technically matured and proven technology. About 97% of the total global ESSs are PHS with an installed capacity of 168 GW [5]. In comparison to the battery ESS (BESS), PHS has a low lifecycle cost, high lifetime, and requires less maintenance [6]. However, in the context of a microgrid, a small capacity PHS with control flexibility is a boon over other ESS [7].

As per the fifth minor irrigation census of India, a growing number of 5500 units of wind and solar powered pumps are in operation [8]. These pumping systems can be configured to obtain pico hydel energy storage (PHES), which resembles the PHS scheme. The term PHES is used to distinguish it from PHS with large reservoirs as its capacity is limited to 5 kW. Various attempts have been made in the past to utilize this concept, however, they have either considered an ideal PHS [9] or a fixed speed PHS [10] with no control flexibility. Furthermore, the previous works were mainly focused on proposing a novel energy management strategy residing on top of the control hierarchy, which leaves a void at the local control level [11]–[13]. To address this gap, the authors of this article have developed a variable-speed PHES with vector control in their previous paper [14]. However, the vector control strategy neither offered the inertial response nor exhibited frequency dependency.

The rotational inertia of the synchronous machines (SMs) is an important entity, which holds the stability of the power system

1937-9234 © 2021 IEEE. Personal use is permitted, but republication/redistribution requires IEEE permission.
See https://www.ieee.org/publications/rights/index.html for more information.

Authorized licensed use limited to: Aalborg Universitetsbibliotek. Downloaded on February 18,2021 at 13:48:56 UTC from IEEE Xplore. Restrictions apply.

This article has been accepted for inclusion in a future issue of this journal. Content is final as presented, with the exception of pagination.

during contingencies [15]. The primary response to any frequency event in the grid is provided by the inertia of large rotors. However, autonomous microgrids are deprived of inertia due to static sources [16]. Although the wind turbines have high rotor inertia, the variable-speed units are perceived as static sources by the grid [17]. This argument is also valid for variable-speed PHS controlled by power converters. Nevertheless, the need for inertia in autonomous and weak grids had paved the way for virtual inertia emulation techniques.

The introduction of droop control techniques for power converters was the first attempt to induce frequency dependency to power converters, but it failed to exhibit inertial response [18]. Subsequently, the virtual SM was developed to exhibit the inertial behavior of SM [19]. However, it relied on current control loops, which makes it similar to the current-controlled converters [20]. Eventually, a virtual synchronous generator was proposed with a short-term ESS to emulate virtual inertia through a frequency derivative term [21]. Various other implementations of virtual inertia emulation were comprehensively reviewed and reported in [22]. Lately, synchronverter was proposed by combining the dc-link capacitor and power converter to mimic virtual inertia [23]. By far, this topology remains the best resemblance of an SM exhibiting all its physical properties. As a bonus, its parameters like inertia, inductances, and the frictional coefficient can be tuned, unlike the physical SM. Ever since, synchronverter was utilized in various applications, such as wind turbines [24], solar photovoltaic (PV) [25], high voltage dc (HVdc) transmission [26], electric vehicle charging [27], and BESS [28].

As far as authors are aware, the synchronverter control is yet to be adapted for the variable-speed PHES. So, as an initial effort, virtual inertia capability is induced into the variable-speed PHES by modifying the synchronverter technology in this article. Thus, the contributions of this article are as follows.

1) A sustainable energy storage with modified synchronverter technology is proposed by reconfiguring the RES powered agricultural pumping systems in India.
2) The small-signal model of the developed PHES is presented along with the eigenvalue analysis to prove the system stability. This approach could also be used to analyze the performance of a large variable-speed PHS with the synchronverter control.
3) The interaction between the droop controlled governor, and the synchronverter control is investigated. The investigation is deemed important due to the frequency dependency of the synchronverter and the droop controlled governor.
4) The effect of parameter variation on the power response of PHES is analyzed through time-domain simulations to support the outcomes of the small-signal analysis.
5) Finally, the performance of variable-speed PHES with synchronverter and vector control is investigated through time-domain simulations to gauge their efficacy.

Subsequently, the modeling of the system components is discussed in Section II, followed by the control aspects of power converters in Section III. The small-signal modeling approach and the eigenvalue analysis are presented in Section IV. Finally, the performance of the proposed strategy is demonstrated in Section V, and the article is concluded in Section VI.

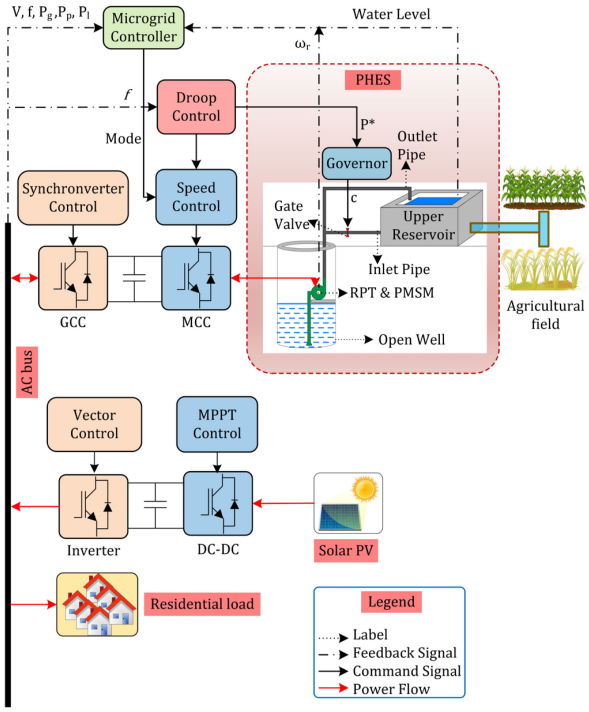

Fig. 1. Microgrid with variable-speed PHES with synchronverter.

II. Modeling of System Components

A. System Description

The microgrid consists of solar PV, PHES, and residential loads, as shown in Fig. 1. The solar PV capacity is 44 kWp, which was assumed as 36 kW at nominal irradiation and the capacity of PHES was 5 kW and 22 kWh. The proposed PHES was formed by an open well, upper reservoir, governor, reversible pump-turbine, and a permanent magnet synchronous machine (PMSM). The available hydraulic head between the open well (lower reservoir) and the upper reservoir was used to mimic the operation of the PHS. This configuration resembled the renewable energy powered agricultural pumping systems widely found across the globe with the energy storage attribute.

The excess energy in the microgrid was stored as hydraulic potential energy through pumping operation. Meanwhile, the deficit in power was injected by PHES operating in generation mode. The pumping and generation operations can be correlated with the charging and discharging of BESS, respectively. A pair of voltage source converters (VSCs) was used to enhance the flexibility of PHES in both modes of operation. The operation modes were decided by the microgrid controller based on the power balance in the microgrid and the water level in the upper reservoir. A minimum level of water in the reservoir is always ensured to cater to the agricultural water demand. Moreover, the capacity of the upper reservoir was computed by taking the irrigation demand into account. The derivation of upper reservoir capacity and the detailed modeling of PHES can be found in the author's previous publication [29]. Furthermore, the worst-case scenarios with no water for power generation can be overridden by backup resources like diesel generators or load shedding

Authorized licensed use limited to: Aalborg Universitetsbibliotek. Downloaded on February 18,2021 at 13:48:56 UTC from IEEE Xplore. Restrictions apply.

This article has been accepted for inclusion in a future issue of this journal. Content is final as presented, with the exception of pagination.

control. However, they are not discussed in this article to confine the scope.

B. Mechanical Components

1) *Hydraulic Turbine*: A nonlinear model of a hydraulic turbine assuming an incompressible flow and negligible water hammer effect was adopted [30]. The rate of change of water discharge in the penstock was derived using the laws of momentum, which yielded (1). The net force acting on the turbine was derived by considering the hydraulic pressure at entry and exit of the penstock of length l_p and sectional area A_p. In (1), ρ_w is the density of water (kg·m^{-3}), g is the acceleration due to gravity (ms^{-1}) and H_s, H_l, H_t are the static head, head loss, and turbine head (m), respectively. The frictional head loss (H_l) was neglected to reduce the complexity, and the nominal values of discharge (Q_{nom}) and head (H_{nom}) were used to derive (2).

$$\rho_w l_p \frac{dQ_t}{dt} = (H_s - H_l - H_t) A_p \rho_w g \tag{1}$$

$$\frac{dq_t}{dt} = \frac{1}{\tau_{ws}} (1 - h_t) \tag{2}$$

where $q_t = \frac{Q_t}{Q_{\text{nom}}}$, $h_t = \frac{H_t}{H_{\text{nom}}}$, $\tau_{ws} = \frac{lQ_{\text{nom}}}{A_p g H_{\text{nom}}}$.

The gate position c_g in (3) was controlled by a servo mechanism to adjust the water discharge rate into the turbine

$$q_t = c_g \sqrt{h_t}. \tag{3}$$

The turbine power output with the damping effect rendered by the movement was given by (4), where D_t represents damping coefficient, $A_t = \eta_t \cdot \rho_w \cdot g$, and η_t represents turbine efficiency

$$P_t = A_t \cdot q_t \cdot h_t - D_t c_g \Delta\omega_t. \tag{4}$$

Thus, the nonlinear model of the hydraulic turbine was represented by (2), (3), (4), and linearizing them will yield (5), (6), (7). Eventually, solving for Δq_t and Δh_t yielded (8) and (9), respectively.

$$\frac{d\Delta q_t}{dt} = -\frac{\Delta h_t}{\tau_{ws}} \tag{5}$$

$$\Delta q_t = \frac{\partial q_t}{\partial c_g}\Delta c_g + \frac{\partial q_t}{\partial h_t}\Delta h_t \tag{6}$$

$$\Delta P_t = \frac{\partial P_t}{\partial h_t}\Delta h_t + \frac{\partial P_t}{\partial q_t}\Delta q_t \tag{7}$$

$$\Delta q_t = -\frac{\Delta h_t}{s\tau_{ws}} \tag{8}$$

$$\Delta h_t = -\frac{\frac{\partial q_t}{\partial c_g}\Delta c_g}{\frac{1}{s\tau_{ws}} + \frac{\partial q_t}{\partial h_t}} \tag{9}$$

$$\frac{\Delta P_t}{\Delta c_g} = \frac{\left(\frac{\partial q_t}{\partial c_g}\frac{\partial P_t}{\partial q_t}\right) - \left(s\tau_{ws}\frac{\partial P_t}{\partial h_t}\frac{\partial q_t}{\partial c_g}\right)}{1 + s\tau_{ws}\frac{\partial q_t}{\partial h_t}} \tag{10}$$

$$\frac{\partial q_t}{\partial h_t} = \frac{1}{2}\frac{c_{g0}}{\sqrt{h_{t0}}}$$

$$\frac{\partial q_t}{\partial c_g} = \sqrt{h_{t0}}$$

$$\frac{\partial P_t}{\partial q_t} = A_t h_{t0}$$

$$\frac{\partial P_t}{\partial h_t} = A_t q_{t0}$$

$$\tau'_{ws} = \tau_{ws}\frac{q_{t0}}{h_{t0}}$$

$$\frac{\Delta P_t}{\Delta c_g} = A_t h_{t0}^{\frac{3}{2}}\left(\frac{1 - s\tau'_{ws}}{1 + \frac{s\tau'_{ws}}{2}}\right) \tag{11}$$

Finally, the relationship between the change in power output to the change in gate position was obtained by substituting (8), (9) into (7). The partial derivatives in (10) were evaluated around an initial point to obtain the linearized first-order model of the hydraulic turbine (11).

2) *Hydraulic Governor:* The hydraulic governor adjusts the water discharged using a servo mechanism to control the power output of the turbine. The governor was combined with a droop control to translate the grid frequency (ω_g) variations to the corresponding power setpoint (ΔP_g^*) (12). Subsequently, the discharge reference (Δq_t^*) from the PI controller (13) was utilized by the servo mechanism to vary the gate position with a mechanical time delay (τ_g) (14). It is also worth mentioning that the power injected into the grid (P_g) was fed back to account for the losses.

$$\Delta P_g^* = D_g \Delta\omega_g \tag{12}$$

$$\Delta q_t^* = \left(K_{pg} + \frac{K_{ig}}{s}\right)\Delta P_g \tag{13}$$

$$\Delta c_g = \frac{1}{\sqrt{h_{t0}}}\left(\frac{1}{1 + s\tau_g}\right)\Delta q_t^* \tag{14}$$

III. Control of Power Converters

A. Virtual Inertia Emulation

The inertia of rotating machines plays a vital role in maintaining the frequency stability of the power system by exchanging the kinetic energy of their rotor. After an under frequency event, the kinetic energy stored in the rotor is released, whereas the kinetic energy is accumulated in the rotor after an over frequency event. Consequently, the frequency transients are curtailed by this continuous exchange of kinetic energy stored in the rotor inertia. The inertia of large interconnected power systems is high due to the high share of conventional generators as opposed to the static RES. Having said that, the inertia decreases when the share of RES is significantly increased, which leaves the microgrids more vulnerable to frequency excursions. Meanwhile, the power converters decouple the inertial response of RES with rotating machines such as wind turbines, which is also applicable to the variable-speed PHES proposed in this article.

A pair of VSC, namely machine control converter (MCC) and grid coupling converter (GCC), were used to control the PHES. As a consequence, the back to back VSC configuration restrained the PMSM to respond to frequency variations, which necessitates inducing virtual inertia capability to PHES. Hence, the synchronverter strategy was modified to control the GCC, while MCC was controlled by field-oriented control (FOC). Since FOC is a well-established technique for speed control of PMSM, it is not discussed here, and the readers are referred to [5].

Authorized licensed use limited to: Aalborg Universitetsbibliotek. Downloaded on February 18,2021 at 13:48:56 UTC from IEEE Xplore. Restrictions apply.

This article has been accepted for inclusion in a future issue of this journal. Content is final as presented, with the exception of pagination.

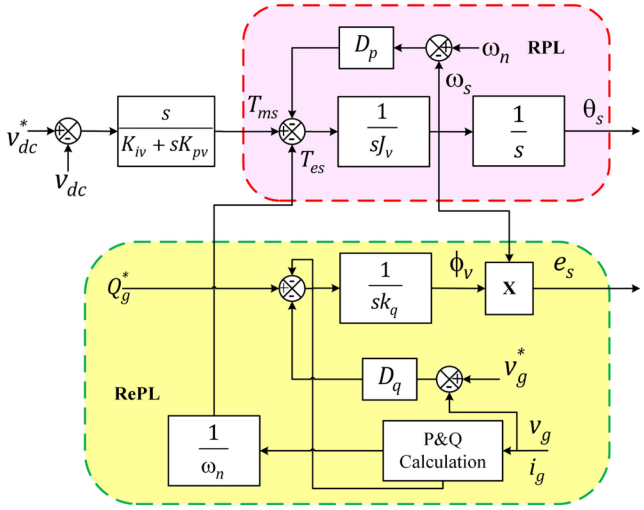

Fig. 2. Proposed synchronverter control with dc-link voltage control.

B. Proposed Synchronverter Control

Synchronverter is a combination of dc-link capacitor and VSC with a novel control algorithm, which mimics an SM. The voltages of the synchronverter in the *dq* frame were derived by applying Kirchhoff's voltage law (15), (16). Aligning the induced voltage of the synchronverter (e_s) (17) with the q axis voltage yielded the real power (18) and reactive power (19) equations. In (15)–(19), ϕ_v, ω_s, R_s, L_s, i_{qs}, and i_{ds} represent virtual flux synchronverter frequency, stator resistance, stator inductance, d and q axis currents, respectively.

$$v_{ds} = e_s - i_{ds}R_s + \omega_s L_s i_{qs} - L_s \frac{di_{ds}}{dt} \tag{15}$$

$$v_{qs} = e_s - i_{qs}R_s - \omega_s L_s i_{ds} - L_s \frac{di_{qs}}{dt} \tag{16}$$

$$e_s = \phi_v \omega_s \tag{17}$$

$$P_s = \frac{3}{2} v_{qs} i_{qs} \tag{18}$$

$$Q_s = \frac{3}{2} v_{qs} i_{ds} \tag{19}$$

The original control architecture of the synchronverter has an independent real power loop (RPL) and reactive power loop, which directly controls the real and reactive power output. However, the control objective of the synchronverter in this article is to regulate the dc-link voltage. Hence, a dc-link voltage controller was augmented with the original synchronverter (see Fig. 2). The real power regulation was realized with the dynamic torque equation of an electromechanical system (20), where, T_{ms}, T_{es}, J_v, D_p, and ω_n represent mechanical torque, electromagnetic torque, virtual inertia, power droop coefficient, and nominal frequency, respectively. The value of T_{ms} was derived from the dc-link voltage controller and T_{es} was derived from the line voltage and current. The torque T_{ms} acted as a reference, and torque T_{es} was regulated by the RPL. Eventually, the frequency of synchronverter (ω_s) was affected by the instantaneous difference between those two torque quantities, thereby regulating the frequency according to (20). In short, the energy stored in the dc-link capacitor is either absorbed or released rapidly by the synchronverter after a frequency event, which mimics the inertial response of SM.

$$\frac{d\omega_s}{dt} = \frac{1}{J_v}\left(T_{ms} - T_{es} - D_p\left(\omega_n - \omega_s\right)\right) \tag{20}$$

$$\frac{d\theta_s}{dt} = \omega_s \tag{21}$$

$$T_{ms} = \left(v^*_{dc} - v_{dc}\right)\left(K_{pv} + \int K_{iv}\right) \tag{22}$$

$$\frac{d\phi_v}{dt} = K_q\left(Q^*_g - Q_g\right) + D_q\left(v^*_g - v_g\right) \tag{23}$$

A PI dc-link voltage controller with integral gain (K_{iv}) and proportional gain (K_{pv}) was augmented to the synchronverter to maintain the dc-link voltage (v_{dc}) to the reference value v^*_{dc} [see (22)]. The dc-link voltage depends on the net active power flow across the capacitor. For instance, the sudden increase in the power generated by PHES will increase the dc-link voltage and vice versa. Hence, the real power flow through the dc-link was controlled by the phase angle (θ_s), whereby regulating the dc-link voltage. Meanwhile, the output voltage magnitude of synchronverter was controlled by the time integral of (23), where K_q, D_q, Q_g, Q^*_g, v_g, and v^*_g represent the reactive power gain, voltage droop coefficient, measured reactive power, reference reactive power, measured line voltage, and reference line voltage, respectively.

IV. Small-Signal Analysis

A. Small-Signal Model

The dc-link coupled the electromechanical system with the synchronverter, and its voltage was affected by power flowing on both sides. Thus, the subsystems were modeled separately and combined using

$$\Delta v_{\mathrm{dc}} = \Delta v^{\mathrm{syn}}_{\mathrm{dc}} + \Delta v^{\mathrm{mec}}_{\mathrm{dc}}. \tag{24}$$

1) *Electromechanical System*: The electromechanical subsystem consists of the hydraulic governor with servo mechanism, hydraulic turbine, electrical machine, and the machine side converter (25), (26). The linearized models presented in Section II were used to derive the closed-loop transfer function of the electromechanical system (27).

$$G_{\mathrm{mec}}(s) = \frac{G_{\mathrm{gov}}(s)\cdot G_{\mathrm{servo}}(s)\cdot G_{\mathrm{turbine}}(s)}{1 + G_{\mathrm{gov}}(s)\cdot G_{\mathrm{servo}}(S)\cdot G_{\mathrm{turbine}}(S)} \tag{25}$$

$$G_{\mathrm{mec}}(s) = \frac{A_t h^3_{t0}\left(\frac{s}{K_{ig}+sK_{pg}}\right)\cdot\left(\frac{1}{1+s\tau_g}\right)\cdot\left(\frac{1-s\tau'_{ws}}{1+\frac{s\tau'_{ws}}{2}}\right)}{1 + A_t h^3_{t0}\left(\frac{s}{K_{ig}+sK_{pg}}\right)\cdot\left(\frac{1}{1+s\tau_g}\right)\cdot\left(\frac{1-s\tau'_{ws}}{1+\frac{s\tau'_{ws}}{2}}\right)} \tag{26}$$

$$G_{\mathrm{mec}}(s) = A_t h^3_{t0}\left(\frac{s - s^2\tau'_{ws}}{As^3 + Bs^2 + Cs + D}\right) \tag{27}$$

$$A = \frac{K_{ig}\tau_g\tau'_{ws}}{2}$$

Authorized licensed use limited to: Aalborg Universitetsbibliotek. Downloaded on February 18,2021 at 13:48:56 UTC from IEEE Xplore. Restrictions apply.

This article has been accepted for inclusion in a future issue of this journal. Content is final as presented, with the exception of pagination.

$$B = K_{pg}\tau_g + \frac{K_{pg}\tau'_{ws} + K_{ig}\tau_g\tau'_{ws}}{2} - A_t h_{t0}^3 \tau'_{ws}$$

$$C = K_{pg} + K_{ig}\tau_g + \frac{K_{ig}\tau'_{ws}}{2} + A_t h_{t0}^3 \; D = K_{ig}$$

The mechanical power was mapped to the dc-link voltage to obtain the transfer function of the electromechanical system. First, the angular speed reference was converted to power reference through a droop coefficient (D_g). Next, the change in power output was related to the voltage across the dc-link capacitor (C_{dc}) by neglecting losses in PMSM and MCC.

$$\Delta v_{\rm dc} = \frac{\Delta i_{\rm dc}}{sC_{\rm dc}} \tag{28}$$

$$\Delta P_t = \Delta P_{\rm dc} = \Delta v_{\rm dc}\Delta i_{\rm dc} \tag{29}$$

$$\Delta v_{\rm dc}^{\rm mec} = \left(\frac{\Delta i_{\rm dc}}{sC_{\rm dc} + q_p}\right) \tag{30}$$

$$\Rightarrow \frac{\Delta P_{\rm dc}}{v_{\rm dc}^{\rm nom}}\left(\frac{1}{sC_{\rm dc} + q_p}\right)$$

$$G_{\rm emec}(s) = \frac{A_t h_{t0}^3}{v_{\rm dc}^{\rm nom}}\left(\frac{s - s^2\tau'_{ws}}{As^3 + Bs^2 + Cs + D}\right) \cdot \left(\frac{1}{sC_{\rm dc} + q_p}\right). \tag{31}$$

2) *Synchronverter*: Since the dc-link voltage was affected only by the real power exchange with the grid, the effect of reactive power loop has been neglected to reduce the order of the system.

$$G_{\rm syn}(s) = G_{v\rm dc}(s) \cdot G_{\rm torque}(s) \cdot G_{ks}(s) \tag{32}$$

$$G'_{\rm syn}(s) = \left(\frac{s}{K_{iv} + sK_{\rm pv}}\right) \cdot \left(\frac{1}{D_p + sJ_v}\right) \cdot \left(\frac{1}{s}\right) \tag{33}$$

By linearizing (20)–(22), and assuming no change in the electromagnetic torque, the transfer function of the torque regulation loop was reduced to (33). The angle θ_s from RPL corresponded to the synchronizing power output of the synchronverter. Thus, the change in dc-link voltage due to the synchronverter was derived using the synchronizing power coefficient ($K_{\rm syn}$)

$$G_{ks}(s) = \left(\frac{K_{\rm syn}}{v_{\rm dc}^{\rm nom}(C_{\rm dc}s + q_p)}\right) \tag{34}$$

$$G_{\rm syn}(s) = \left(\frac{1}{\alpha s^2 + \beta s + \gamma}\right) \cdot \left(\frac{K_{\rm syn}}{v_{\rm dc}^{\rm nom}(C_{\rm dc}s + q_p)}\right) \tag{35}$$

where $\alpha = K_{\rm pv}J_v$; $\beta = K_{iv}J_v + K_{pv}D_p$; $\gamma = K_{iv}D_p$

$$\left.\frac{\Delta v_{\rm dc}}{\Delta\omega_g}\right|_{\Delta v_{\rm dc}^{\rm nom}=0} = \frac{G_{\rm emec}(s)}{1 + G_{\rm syn}(s)}. \tag{36}$$

Eventually, the small-signal model of the complete system represents the influence of different subsystems on dc-link voltage (see Fig. 3). The nominal dc-link voltage $v_{\rm dc}^{\rm nom}$ remained constant, while only the disturbance from the electromechanical subsystem was considered. Hence, the model was reduced to a single input and single-output model with unity forward gain and synchronverter gain in the feedback loop (36) (see Fig. 4).

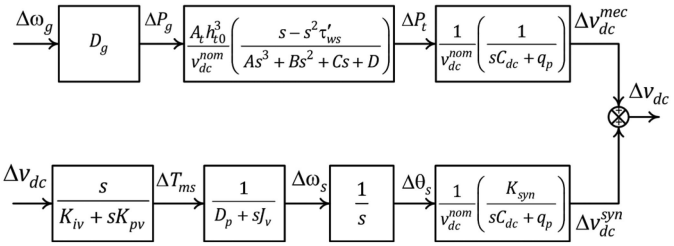

Fig. 3. Small-signal model of PHES with synchronverter control.

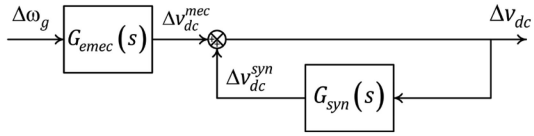

Fig. 4. Single-input and single-output model of PHES with synchronverter control.

B. Eigenvalue Analysis

The small-signal stability of the system is often affected by the system parameters, controller gains, and control variables. Hence, the critical parameters such as virtual inertia J_v, droop coefficient D_p, and the governor time constant τ_g were varied to assess the stability of the system.

1) *Variation of D_p*: The value of D_p was determined by considering the amount of power change (P_g) required during the grid frequency (f) excursions, which usually varies from 3% to 5% (37). Subsequently, the system stability was examined by sweeping D_p from 10 to 500. The trace of eigenvalues demonstrated that the system was stable during the variation and the dominant poles $\lambda_3 - \lambda_6$ laid closer to the imaginary axis [see Fig. 5(a)]. Meanwhile, for an increase in D_p, the dominant poles $\lambda_3 - \lambda_6$ moved toward the origin, whereas the real poles λ_7, λ_8 moved toward $-\infty$. However, only the poles λ_3, λ_4 contributed to oscillation damping, as given in Table I.

$$D_p = \frac{\%P_g P_n}{\%f\omega_n^2} \tag{37}$$

where P_n and ω_n are nominal power and frequency.

2) *Variation of J_v*: The value of virtual inertia (J_v) dictated the rate of change of frequency (ROCOF). A larger value reduced the ROCOF, while resulted in a slow rate of frequency recovery. So, a tradeoff should be met between ROCOF and the frequency recovery rate. Meanwhile, the maximum value of J_v was limited by the size of the dc-link capacitor (38) and practically constrained by (39).

$$J_{v,\max} = \frac{C_{\rm dc}V_{\rm dc}^2}{\omega_n^2} \tag{38}$$

$$1 \le \frac{J_v\omega_n^2}{P_n} \le 12 \tag{39}$$

The value of J_v was varied from 0.5 to 15 kg·m^2, and the eigenvalues were traced [see Fig. 5(b)]. The dominant poles λ_3, λ_4 moved toward the origin and remained within the left half of *S* plane. The movement toward the origin increased the response time, which is the anticipated behavior. However, the complex conjugates λ_3, λ_4 did not have a significant effect on system damping, which is evident from Table I. However, the

Authorized licensed use limited to: Aalborg Universitetsbibliotek. Downloaded on February 18,2021 at 13:48:56 UTC from IEEE Xplore. Restrictions apply.

This article has been accepted for inclusion in a future issue of this journal. Content is final as presented, with the exception of pagination.

TABLE I
EFFECT OF PARAMETER VARIATION ON THE DOMINANT OSCILLATORY MODES OF THE DC-LINK VOLTAGE

Parameters		Eigenvalue		Damping ratio		Undamped frequency (rad/s)		Damped frequency (rad/s)	
		λ_1,λ_2	λ_3,λ_4	λ_1,λ_2	λ_3,λ_4	λ_1,λ_2	λ_3,λ_4	λ_1,λ_2	λ_3,λ_4
J_v = *1.5*	D_p =10	-37.42 ± 47.16i	-0.14 ± 2.81i	0.62	0.05	60.20	2.814	47.16	2.811
τ_g =0.02	D_p =500	-37.42 ± 47.16i	-2.26 ± 9.44i	0.62	0.23	60.20	9.71	47.16	9.44
D_p =100	J_v =1.5	-37.42 ± 47.16i	-0.21 ± 3.98i	0.62	0.05	60.20	3.985	47.16	3.98
τ_g =0.02	J_v =15	-37.42 ± 47.16i	-0.58 ± 3.62i	0.62	0.16	60.20	3.67	47.16	3.62
D_p =100	τ_g =0.02	-37.42 ± 47.16i	-0.21 ± 3.98i	0.62	0.05	60.20	3.985	47.16	3.98
J_v = *1.5*	τ_g =0.1	-29.76 ± 23.32i	-0.21 ± 3.98i	0.78	0.05	37.80	3.985	23.31	3.98

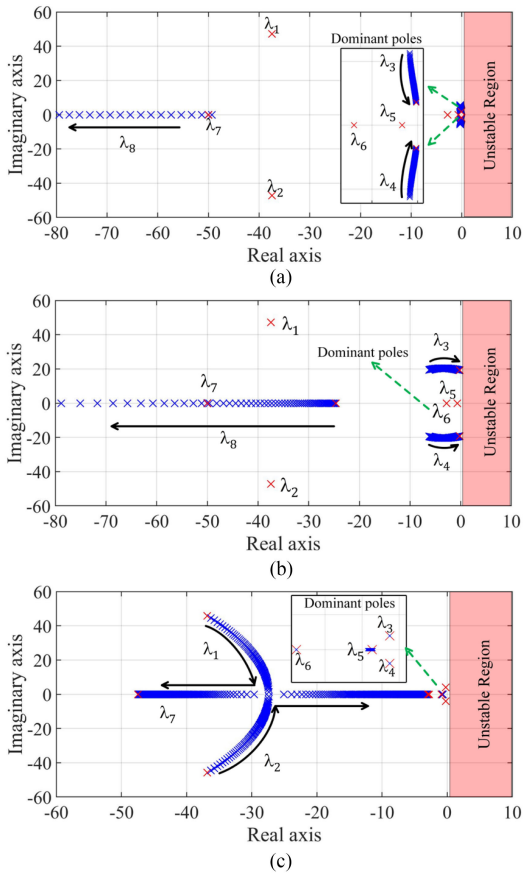

Fig. 5. Eigenvalue traces with variation in (a) D_p. (b) J_v. (c) τ_g.

frequency of oscillation initially increased and then decreased after a critical value of J_v. Meanwhile, the movement of real poles λ_7, λ_8 toward $-\infty$ was not significant as they did not contribute to the damping of oscillations.

3) *Variation of* τ_g: The governor time constant (τ_g) has also contributed to the oscillatory modes of dc-link voltage. Hence, its effect on system stability was analysed to exemplify its interaction with the synchronverter. The value of τ_g was varied within a range of 0.02 to 0.4 s, and the eigenvalues were traced [see Fig. 5(c)]. Subsequently, for an increase in τ_g, the dominant poles λ_5, λ_6 moved toward the origin, which increased the system response time. However, the complex conjugate poles λ_1, λ_2 became real and moved in the opposite direction after a critical value of τ_g. Thus, τ_g can be controlled to damp the system oscillations up to a critical value (see Table I). Meanwhile, a few dominant poles λ_3, λ_4 which laid closer to the origin did not show a considerable effect for the change in τ_g.

4) *Governor and Synchronverter Interaction*: The frequency dependency of the governor and synchronverter demanded an investigation on probable interaction between them. Moreover, the governor time constant and the virtual inertia had similar characteristics of delaying the real power change. Hence, the interaction was inferred from the traces of eigenvalues presented. A pair of complex conjugate poles λ_1, λ_2 and real poles λ_5, λ_6 corresponding to τ_g remained unaffected for the variation in D_p and J_v. However, these poles moved toward the origin only for the variation in τ_g. Subsequently, the oscillatory frequency was reduced with an increase in τ_g due to the effect of complex conjugate poles λ_1, λ_2 (see Table I). Thus, the analysis revealed no interaction between the governor and synchronverter under the considered scenario.

TABLE II
PARAMETERS OF SYSTEM COMPONENTS

Parameters	Value
Turbine Power	5 kW
Upper reservoir volume	450 m^3
Energy storage capacity	22 kWh
Rated head	17-20 m
Rated discharge	25-30 l/s
dc-link capacitor	2.5 mF
J_v , D_p , τ_g	2 $kg.m^2$, 200, 0.05 s
Switching frequency	5 kHz
LCL filter	11 mH, 0.62 μF, 6.6 mH
Line inductance, resistance	0.0238 Ω/km, 0.342 Ω/km

V. PERFORMANCE ANALYSIS

The effectiveness of the proposed control strategy was validated through time-domain simulations executed in MATLAB/Simulink under various scenarios, such as load change, irradiation change, and fault at the terminals. The performance of PHES was compared with the classical vector and synchronverter control, followed by the effects of parameter variation on the system response. The parameters used for simulation can be found in Table II.

Authorized licensed use limited to: Aalborg Universitetsbibliotek. Downloaded on February 18,2021 at 13:48:56 UTC from IEEE Xplore. Restrictions apply.

This article has been accepted for inclusion in a future issue of this journal. Content is final as presented, with the exception of pagination.

A. Generation Mode

1) *Load and Irradiation Change*: In this case, the performance was analyzed by switching the loads in the microgrid and changing the irradiation input to the solar PV system. The first transition was at $t = 10$ s, where the load was switched from 36 to 39 kW, while the solar PV power remained constant at 34 kW [see Fig. 6(f)]. Subsequently, for the second transition, the solar irradiation was increased from 845 to 900 W/m2 at $t = 20$ s [see Fig. 6(e)], while the load was maintained at 39 kW. To mimic the real-time scenario, the instantaneous irradiation input to the solar PV system was generated with random variations.

During the initial 10 s, there was a deficit of 2 kW which was fed by PHES to maintain the microgrid frequency. The vector control had high initial transients in the real power characteristics with a peak overshoot of 4000 W, in contrast to 3050 W with the synchronverter control [see Fig. 6(a)]. Similarly, the vector control had a higher settling time of 5 s, as opposed to 3 s with synchronverter control. A similar response was perceived in the reactive power output, where the vector control had a higher settling time of 6 s [see Fig. 6(b)]. Notably, the reactive power was controlled to maintain the power factor of the microgrid between 0.98 to 1 in all the cases henceforth.

The initial transients in the water discharge characteristics were more pronounced with vector control, where the peak overshoot was approximately 0.04 m^3s^{-1}. Whereas the peak overshoot was limited to 0.025 m^3s^{-1} with synchronverter control [see Fig. 6(c)]. In contrast to other characteristics, the dc-link voltage reached the reference value of 600 V in 0.1 s with vector control, while the synchronverter took 4 s due to its dependence on dc-link properties (38) [see Fig. 6(d)].

After the first transition, the sudden change in load was absorbed by PHES, where the synchronverter exhibited a smooth transition, thanks to its inertial response [see Fig. 6(a)]. It is worth mentioning that there was an offset of about 80 var with vector control, which deteriorated the power factor of the system [see Fig. 6(b)]. Meanwhile, steady-state oscillations were observed in the discharge characteristics with vector control, which could induce vibrations and degrade the lifetime of mechanical components [see Fig. 6(c)].

The dc-link voltage, on the other hand, remained stable with the vector control and exhibited a step change with the synchronverter control. However, the dc-link voltage remained within an anticipated limit of $\pm 5\%$ [see Fig. 6(d)]. After the second transition, the solar PV output was increased due to an increase in the irradiation input. Consequently, PHES reduced its power output from 5 to 3 kW, thereby regulating the frequency of the microgrid. In all the above cases, the synchronverter control offered a flat frequency regulation compared to the vector control [see Fig. 6(g)].

2) *Fault Analysis*: In this case, a 10 ms three-phase to ground fault was applied at the load terminals at $t = 5$ s, for analyzing the stability of the system during contingencies. The irradiation input to the solar PV system was maintained at a mean value of 800 W/m2 [see Fig. 7(e)], which resulted in PV output of 32 kW [see Fig. 7(f)]. Meanwhile, the load on the system was 37 kW [see Fig. 7(f)], where the deficit of 5 kW was injected by PHES [see Fig. 7(a)]. After the fault, the frequency nadir was curtailed to 49.95 Hz

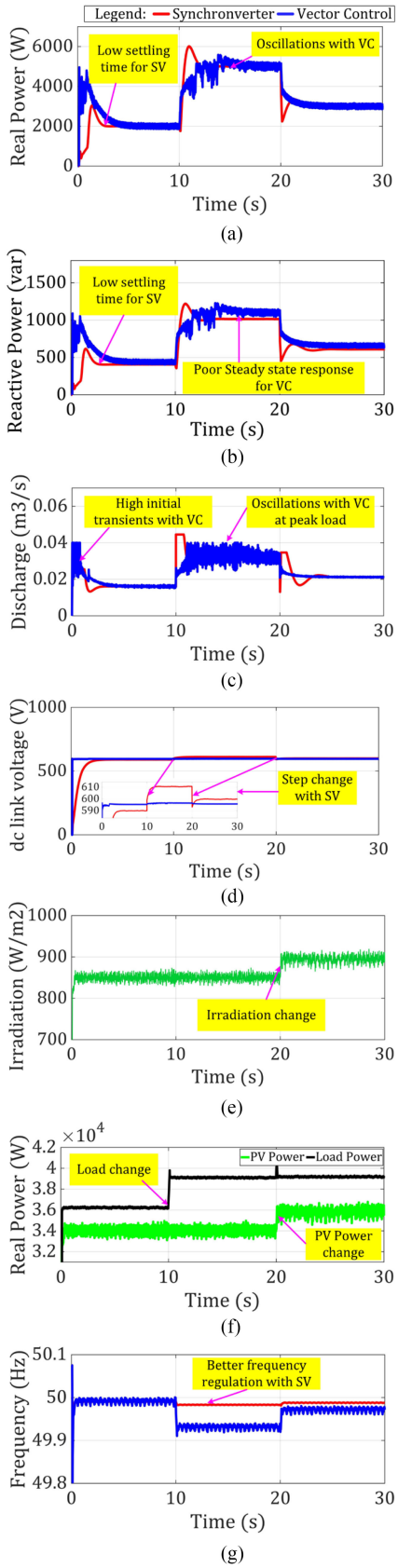

Fig. 6. Comparison of synchronverter and vector control in generation mode of PHES. (a) PHES real power. (b) PHES reactive power. (c) Water discharge rate. (d) PHES dc-link voltage. (e) Solar irradiation. (f) Solar PV output and load power. (g) Microgrid frequency. Note: Henceforth, in all the figures, SV and VC represent synchronverter and vector control, respectively.

Authorized licensed use limited to: Aalborg Universitetsbibliotek. Downloaded on February 18,2021 at 13:48:56 UTC from IEEE Xplore. Restrictions apply.

This article has been accepted for inclusion in a future issue of this journal. Content is final as presented, with the exception of pagination.

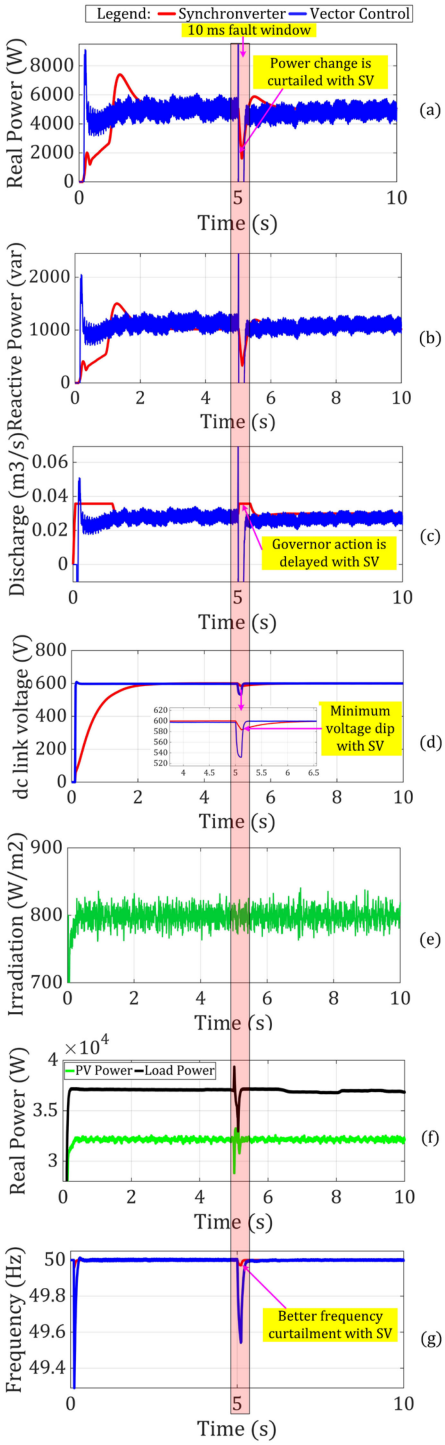

Fig. 7. Comparison of synchronverter and vector control subjected to three-phase to ground fault in generation mode of PHES. (a) PHES real power. (b) PHES reactive power. (c) Water discharge rate. (d) PHES dc-link voltage. (e) Solar irradiation. (f) Solar PV output and load power. (g) Microgrid frequency.

with the synchronverter control, whereas the frequency plummeted with the vector control resulting in a frequency nadir of 49.57 Hz [see Fig. 7(g)].

Meanwhile, the dc-link voltage exhibited a sudden dip with vector control, while there was no considerable change with synchronverter control [see Fig. 7(d)]. Similarly, a sudden dip was observed in the real power [see Fig. 7(a)], reactive power [see Fig. 7(b)], and water discharge characteristics [see Fig. 7(c)] with vector control.

On the other hand, the sudden change in the aforementioned characteristics was curtailed with the synchronverter control, which validated the effectiveness of emulating virtual inertia in the microgrid.

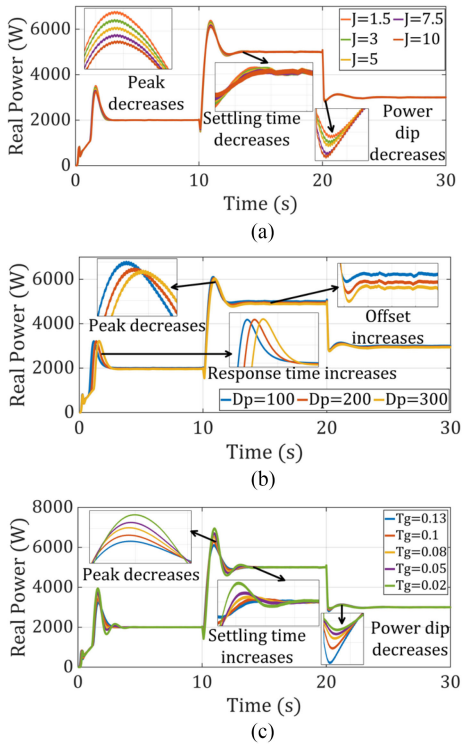

Fig. 8. Effect of increasing the parameter on the real power output in generation mode. (a) Virtual inertia J_v. (b) Droop coefficient D_p. (c) Governor time constant τ_g.

3) *Effect of Parameter Variation:* Although the effect of parameter variation was already illustrated with eigenvalue analysis, its physical significance can be well appreciated by observing the real power response. First, the virtual inertia J_v was swept from 1.5 to 10 kg·m^2 [see Fig. 8(a)]. The initial peak overshoot was reduced from 3500 to 3250 W, and overshoot after the transition was reduced from 6380 to 6300 W for an increase in J_v. However, the settling time increased from 4.2 to 3.5 s for a decrease in J_v due to poor damping. Furthermore, the dip in power decreased from 2800 to 2950 W for an increase in J_v. Thus, an increase in virtual inertia reduced the peak overshoot, dip, and settling time. Subsequently, the droop coefficient D_p was increased from 100 to 300, eventually, the response time increased from 2.2 to 3.1 s [see Fig. 8(b)]. After the first transition, the peak overshoot decreased from 6180 to 6000 W for an increase in D_p, which revealed that it also contributed to the system damping. However, on the downside, the variation also increased the steady-state error by 200 W for the specified variation range. Therefore, it can be concluded that the droop and damping characteristics

Authorized licensed use limited to: Aalborg Universitetsbibliotek. Downloaded on February 18,2021 at 13:48:56 UTC from IEEE Xplore. Restrictions apply.

This article has been accepted for inclusion in a future issue of this journal. Content is final as presented, with the exception of pagination.

of synchronverter are coupled to each other by the control variable D_p.

Next, the value of τ_g was adjusted over a practical range of 0.02 to 0.13 s [see Fig. 8(c)]. The initial transients indicated a decrease in peak overshoot from 3950 to 3250 W for an increase in τ_g. Similarly, after the first transition, the peak overshoot decreased from 6950 to 6100 W. The underlying reason for such behavior is, the large τ_g does not allow instantaneous change in the water discharge rate for a sudden change in power. Meanwhile, when τ_g= 0.02 s, the settling time was higher (5 s) as opposed to τ_g= 0.13, which had 3 s, due to the poor damping offered by small τ_g.

During the second transition, the power dip decreased from 2800 to 2950 W for an increase in τ_g. Nevertheless, these characteristics were congruent to the characteristics obtained with the variation of J_v. Since, the increase in τ_g increases the response time of PHES, which will affect the frequency of the microgrid. For instance, the instantaneous response to the change in system frequency is ensured by a small value of τ_g, while the system oscillations are damped for a large value of τ_g. Hence, the variation of τ_g also affects the system inertia, which is one of the important outcomes of this article. However, a tradeoff should be met between the response time and system damping while varying τ_g.

B. Pumping Mode

1) *Load and Irradiation Change*: Similar to the case explained in the generation mode, the performance in pumping mode was analyzed by switching the loads and changing the irradiation input to the solar PV system. The first transition was at t = 10 s, where the load was switched from 29 to 30 kW [see Fig. 9(f)]. Subsequently, the second transition was induced by changing the irradiation from 850 to 825 W/m^2 at t = 20 s, while the load was maintained constant at 30 kW [see Fig. 9(e)]. It should be noted that PHES can only offer 30% flexibility in pumping mode, since 60% to 70% of the rated power is required for adequate pumping. So, the changes induced in the system are minimum, which is approximately in the range of 5 to 3 kW. Similar to the generation mode, the power absorbed should not increase or decrease abruptly. So, it is rational to analyze whether the synchronverter exhibits similar behavior in pumping mode.

The initial power response showed that synchronverter control had a higher settling time of 4.8 s versus 0.5 s with the vector control. This argument suits both the real and reactive power characteristics [see Fig. 9(a) and (b)]. During the first transition, the solar PV generation was 34 kW, and the load was 30 kW, which resulted in 4 kW excess power in the microgrid. It was absorbed by PHES, whereby the real and reactive power exhibited a smooth variation and had a longer settling time of 2.5 s against vector control, which had 0.2 s. Meanwhile, there were steady-state oscillations observed in the real power characteristics with the vector control, which could lead to potential mechanical oscillations in the shaft.

After the second transition, the power output of solar PV decreased from 34 to 33 kW, which left an excess of 3 kW in the microgrid. Consequently, PHES gradually reduced its power consumption from the grid from 4 to 3 kW with synchronverter

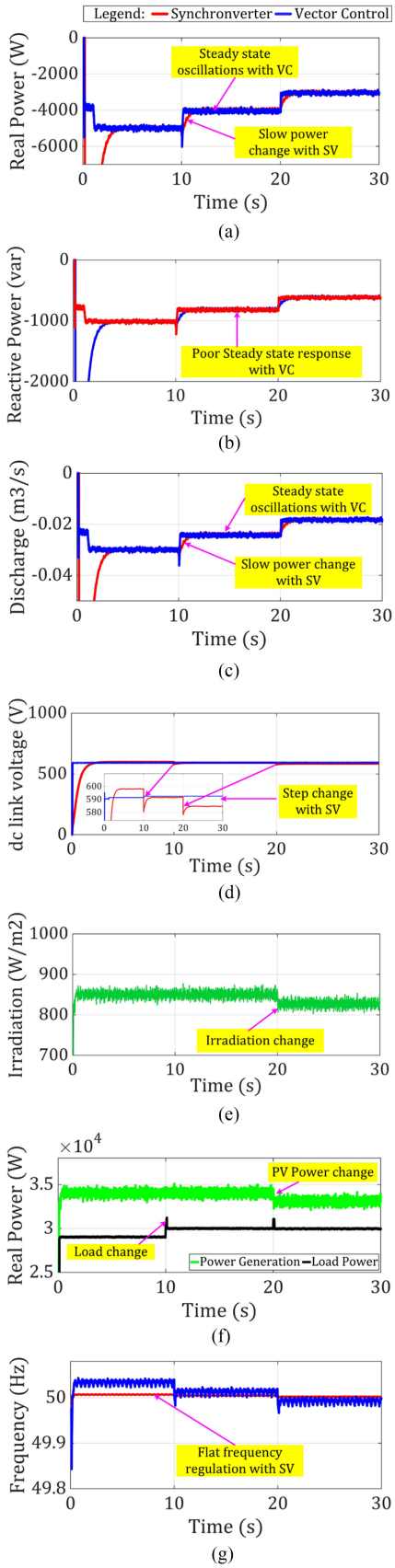

Fig. 9. Comparison of synchronverter and vector control in pumping mode of PHES. (a) PHES real power (b) PHES reactive power. (c) Water discharge rate. (d) PHES dc-link voltage. (e) Solar irradiation. (f) Solar PV output and load power. (g) Microgrid frequency.

Authorized licensed use limited to: Aalborg Universitetsbibliotek. Downloaded on February 18,2021 at 13:48:56 UTC from IEEE Xplore. Restrictions apply.

This article has been accepted for inclusion in a future issue of this journal. Content is final as presented, with the exception of pagination.

control [see Fig. 9(a)]. The water discharge characteristics were proportional to the real power absorbed due to the absence of the governor action [see Fig. 9(c)]. A smooth transition was observed from one value to the other with synchronverter control, in contrast to the vector control. Nevertheless, the steady-state oscillations present in the discharge characteristics could cause oscillations in the water column. Besides all these arguments, the vector control exhibited superior performance in maintaining the dc-link voltage in pumping mode also [see Fig. 9(d)].

During the transition, the synchronverter control showed a step change according to a decrease or increase in the power flow. A variation from 600 to 590 V and 590 to 585 V were observed during the first and second transitions, respectively. However, the voltage variation observed with synchronverter control was within the range of $\pm 5\%$, which was similar to the response observed in generation mode. Furthermore, the synchronverter control offered a flat frequency regulation, while the frequency response with vector control indicated abrupt change during the transients [see Fig. 9(g)].

2) *Fault analysis*: In this scenario, a 10 ms three-phase to ground fault was applied at the load terminals at $t = 5$ s to analyze the pumping mode performance of PHES during contingencies. The irradiation input to the solar PV system was maintained at a mean value of 900 W/m^2 [see Fig. 10(e)], which yielded a power output of 36 kW [see Fig. 10(f)]. The load was maintained at 31 kW [see Fig. 10(d)], which left an excess of 5 kW to be absorbed by PHES [see Fig. 10(a)]. After the fault, the frequency nadir was curtailed to 49.9 Hz with synchronverter control, whereas the frequency nadir slumped to 49.6 Hz with vector control [see Fig. 10(g)]. Besides that, synchronverter control also offered a flat frequency response as opposed to vector control.

Meanwhile, the synchronverter control offered a minimum dip in the dc-link voltage versus a significant dip to 530 V with vector control [see Fig. 10(d)]. Similarly, the real and reactive power changes [see Fig. 10(a) and (b)] were curtailed efficiently with synchronverter control, while the vector control could not curtail the sudden changes. Furthermore, the water discharge characteristics also exhibited a gradual change with synchronverter control, in contrast to characteristics with the vector control after the fault was applied [see Fig. 10(c)].

3) *Effect of Parameter Variation*: The pumping mode performance of PHES was analyzed only with the variation of J_v and $D_p$due to the absence of the governor action. First, J_v was varied over a range of 1.5 to 10 kg·m^2, and the real power response was analyzed [see Fig. 11(a)]. After the first transition, the power dip decreased with an increase in J_v, which was the expected behavior. On reaching the steady-state, an offset of 100 W was observed for an increase in J_v. Moreover, the curves corresponding to $J_v > 3$ kg·m^2 were superimposed with the curve corresponding to $J_v = 10$ kg·m^2. After the second transition, the response time increased by 0.1 s for the same amount of increase in J_v. Thus, the effect of variation of virtual inertia remained analogous for generation and pumping mode. However, the effect was less pronounced in pumping mode as compared to generation mode. It is also worth mentioning that there was no oscillatory response observed in the power response of pumping mode.

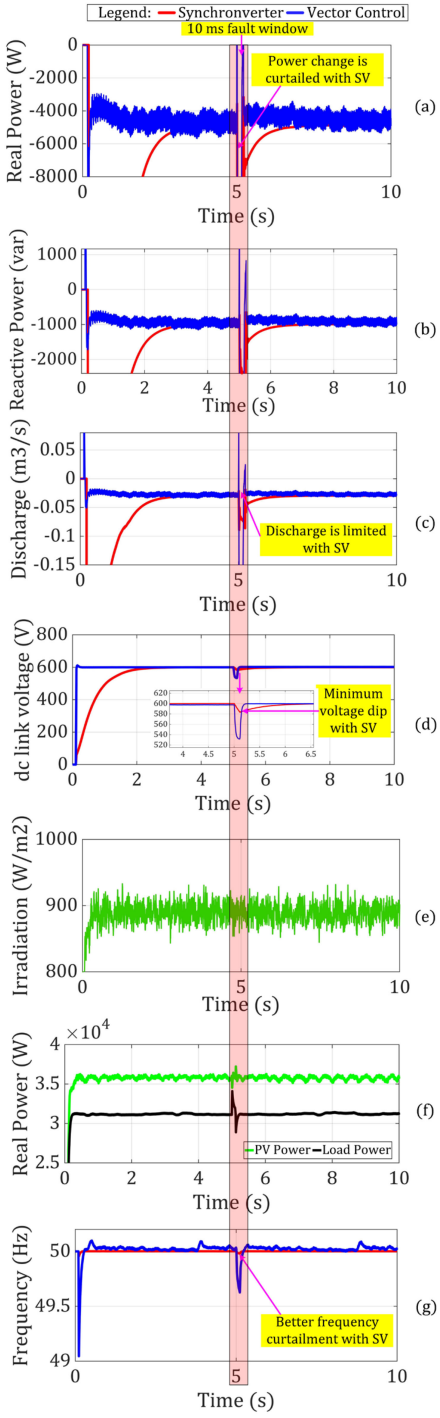

Fig. 10. Comparison of synchronverter and vector control subjected to three-phase to ground fault in pumping mode of PHES. (a) PHES real power. (b) PHES reactive power. (c) Water discharge rate. (d) PHES *dc-link* voltage. (e) Solar irradiation. (f) Solar PV output and load power. (g) Microgrid frequency.

Second, D_p was varied over a range of 100 to 300, and the change in real power response was observed [see Fig. 11(b)]. The response time was not affected considerably, as compared to the generation mode. However, an offset of 50 W was observed for every step variation in D_p. Hence, the variation in D_p did not exhibit considerable effect in pumping mode. Briefly, it can be presumed that the effect of parameter variation had a substantial effect only in the generating mode.

Authorized licensed use limited to: Aalborg Universitetsbibliotek. Downloaded on February 18,2021 at 13:48:56 UTC from IEEE Xplore. Restrictions apply.

This article has been accepted for inclusion in a future issue of this journal. Content is final as presented, with the exception of pagination.

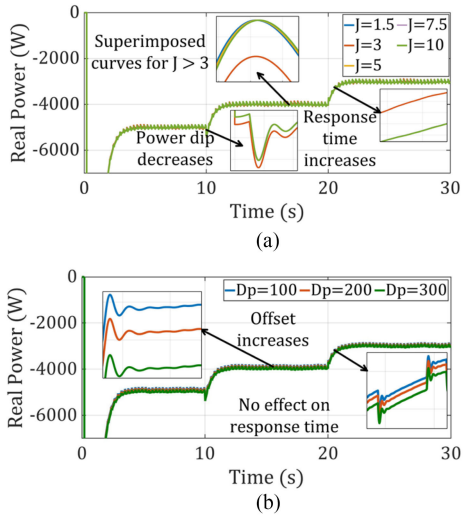

Fig. 11. Effect of increasing the parameter on the real power output in pumping mode. (a) Virtual inertia J_v (b) Droop coefficient D_p.

VI. Conclusion

Autonomous microgrids are technically and economically feasible solution for powering the underprivileged rural communities in India. However, a sustainable ESS with the minimum operation and maintenance intervention is required to ensure the stability of such microgrids. The proposed variable-speed PHES is one such alternative to BESS when the resources are available. Furthermore, the main objective of this article was to induce virtual inertia capability to the proposed PHES and analyze its stability under various circumstances. First, detailed small-signal modeling of the system was presented, and the stability was investigated through eigenvalue analysis. Subsequently, the superiority of proposed synchronverter control over the classical vector control was proved using time-domain simulations carried out in MATLAB/Simulink.

The key outcomes of this article are as follows.

1) The small-signal analysis proved that there was no interaction between the operation of the governor and the synchronverter. Meanwhile, the system remained stable under the variation of key control parameters. It is also worth mentioning that the same approach can be used to model and control large variable-speed PHS with the synchronverter control.
2) The synchronverter control outweighed the performance of vector control in generation and pumping modes by limiting peak overshoot and steady-state oscillations. Nevertheless, the lifetime of mechanical components can be preserved with synchronverter control, which exhibited smooth water discharge characteristics.
3) The governor time constant and the virtual inertia of the synchronverter exhibited a similar real power response. Thus, the governor time constant can be independently varied to improve the inertial response of the system to a certain extent.
4) The parameter variation had considerable effects only in the generation mode and did not affect the pumping mode characteristics. However, the synchronverter control limited the sudden absorption of power from the microgrid in pumping mode.

References

[1] "Pradhan mantri sahaj har ghar yojana (SAUBHAGYA)," Ministry of Power, Government of India, 2020. Accessed: May 15, 2020. [Online]. Available: https://saubhagya.gov.in/dashboard
[2] S. L. Ridgway, J. L. Dooley, and R. P. Hammond, "Large energy storage systems for utilities," *Appl. Energy*, vol. 6, no. 2, pp. 133–142, 1980.
[3] M. Ahmadi, M. E. Lotfy, R. Shigenobu, A. M. Howlader, and T. Senjyu, "Optimal sizing of multiple renewable energy resources and PV inverter reactive power control encompassing environmental, technical, and economic issues," *IEEE Syst. J.*, vol. 13, no. 3, pp. 3026–3037, Sep. 2019.
[4] T. Berger, "Practical constraints for photovoltaic appliances in rural areas of developing countries: Lessons learnt from monitoring of stand-alone systems in remote health posts of north gondar zone, Ethiopia," *Energy Sustain. Develop.*, vol. 40, pp. 68–76, 2017.
[5] K. R. Vasudevan, V. K. Ramachandaramurthy, G. Venugopal, J. B. Ekanayake, and S. K. Tiong, "variable-speed pumped hydro storage: A review of converters, controls and energy management strategies," *Renew. Sustain. Energy Rev.*, vol. 135, 2021, Art. no. 110156.
[6] T. Ma, H. Yang, and L. Lu, "Feasibility study and economic analysis of pumped hydro storage and battery storage for a renewable energy powered island," *Energy Convers. Manag.*, vol. 79, pp. 387–397, 2014.
[7] S. P. Koko, K. Kusakana, and H. J. Vermaak, "Optimal power dispatch of a grid-interactive micro-hydrokinetic-pumped hydro storage system," *J. Energy Storage*, vol. 17, pp. 63–72, 2018.
[8] 5th Census of Minor Irrigation Schemes Report, November. Government of India, Ministry of Water Resources, River Development and Ganga Rejuvenation, 2017.
[9] A. T. Thankappan, S. P. Simon, P. S. Rao Nayak, K. Sundareswaran, and N. P. Padhy, "Pico-hydel hybrid power generation system with an open well energy storage," *IET Gener. Transmiss. Distrib.*, vol. 11, no. 3, pp. 740–749, 2017.
[10] B. S. Pali and S. Vadhera, "An innovative continuous power generation system comprising of wind energy along with pumped-hydro storage and open well," *IEEE Trans. Sustain. Energy*, vol. 11, no. 1, pp. 145–153, Jan. 2020.
[11] N. Mousavi, G. Kothapalli, D. Habibi, C. K. Das, and A. Baniasadi, "Modelling, design, and experimental validation of a grid-connected farmhouse comprising a photovoltaic and a pumped hydro storage system," *Energy Convers. Manag.*, vol. 210, 2020, Art. no. 112675.
[12] T. T. Anilkumar, S. P. Simon, and N. P. Padhy, "Residential electricity cost minimization model through open well-pico turbine pumped storage system," *Appl. Energy*, vol. 195, pp. 23–35, 2017.
[13] S. P. Koko, K. Kusakana, and H. J. Vermaak, "Optimal energy management of a grid-connected micro-hydrokinetic with pumped hydro storage system," *J. Energy Storage*, vol. 14, pp. 8–15, 2017.
[14] V. Krishnakumar R., K. R. Vigna, V. Gomathi, J. B. Ekanayake, and S. K. Tiong, "Modelling and simulation of variable-speed pico hydel energy storage system for microgrid applications," *J. Energy Storage*, vol. 24, Aug. 2019.
[15] M. Saeedian, B. Eskandari, S. Taheri, M. Hinkkanen, and E. Pouresmaeil, "A control technique based on distributed virtual inertia for high penetration of renewable energies under weak grid conditions," *IEEE Syst. J.*, to be published.
[16] B. M. Eid, N. A. Rahim, J. Selvaraj, and A. H. El Khateb, "Control methods and objectives for electronically coupled distributed energy resources in microgrids: A review," *IEEE Syst. J.*, vol. 10, no. 2, pp. 446–458, Jun. 2016.
[17] Y. Wang, J. Meng, X. Zhang, and L. Xu, "Control of PMSG-Based wind turbines for system inertial response and power oscillation damping," *IEEE Trans. Sustain. Energy*, vol. 6, no. 2, pp. 565–574, Apr. 2015.
[18] F. Katiraei and M. R. Iravani, "Power management strategies for a microgrid with multiple distributed generation units," *IEEE Trans. Power Syst.*, vol. 21, no. 4, pp. 1821–1831, Nov. 2006.
[19] H. P. Beck and R. Hesse, "Virtual synchronous machine," in *Proc. 9th Int. Conf. Elect. Power Qual. Utility*, 2007.
[20] X. Hou, Y. Sun, X. Zhang, J. Lu, P. Wang, and J. M. Guerrero, "Improvement of frequency regulation in VSG-based AC microgrid via adaptive virtual inertia," *IEEE Trans. Power Electron.*, vol. 35, no. 2, pp. 1589–1602, Feb. 2020.

Authorized licensed use limited to: Aalborg Universitetsbibliotek. Downloaded on February 18,2021 at 13:48:56 UTC from IEEE Xplore. Restrictions apply.

This article has been accepted for inclusion in a future issue of this journal. Content is final as presented, with the exception of pagination.

[21] J. Driesen and K. Visscher, "Virtual synchronous generators," in *Proc. IEEE Power Energy Soc. 2008 Gen. Meeting Convers. Del. Elect. Energy 21st Century*, 2008, pp. 1–3.
[22] H. Bevrani, T. Ise, and Y. Miura, "Virtual synchronous generators: A survey and new perspectives," *Int. J. Elect. Power Energy Syst.*, vol. 54, pp. 244–254, 2014.
[23] Q. C. Zhong and G. Weiss, "Synchronverters: Inverters that mimic synchronous generators," *IEEE Trans. Ind. Electron.*, vol. 58, no. 4, pp. 1259–1267, Apr. 2011.
[24] W. Yan, L. Cheng, S. Yan, W. Gao, and D. W. Gao, "Enabling and evaluation of inertial control for PMSG-WTG using synchronverter with multiple virtual rotating masses in microgrid," *IEEE Trans. Sustain. Energy*, vol. 11, no. 2, pp. 1078–1088, Apr. 2020.
[25] S. Mishra, D. Pullaguram, S. A. Buragappu, and D. Ramasubramanian, "Single-phase synchronverter for a grid-connected roof top photovoltaic system," *IET Renew. Power Gener.*, vol. 10, no. 8, pp. 1187–1194, 2016.
[26] R. Aouini, B. Marinescu, K. B. Kilani, and M. Elleuch, "Synchronverter-Based emulation and control of HVDC transmission," *IEEE Trans. Power Syst.*, vol. 31, no. 1, pp. 278–286, Jan. 2016.
[27] D. Liu, Q. Zhong, Y. Wang, and G. Liu, "Modeling and control of a V2G charging station based on synchronverter technology," *CSEE J. Power Energy Syst.*, vol. 4, no. 3, pp. 326–338, 2018.
[28] J. Roldan-Perez, A. Rodriguez-Cabero, and M. Prodanovic, "Harmonic virtual impedance design for parallel-connected grid-tied synchronverters," *IEEE J. Emerg. Sel. Top. Power Electron.*, vol. 7, no. 1, pp. 493–503, Mar. 2019.
[29] K. R. Vasudevan, V. K. Ramachandaramurthy, G. Venugopal, J. B. Ekanayake, and S. K. Tiong, "Hierarchical frequency control framework for a remote microgrid with pico hydel energy storage and wind turbine," *Int. J. Elect. Power Energy Syst.*, vol. 127, 2021, Art. no. 106666.
[30] Working group on prime mover and energy supply, "Hydraulic turbine and turbine control models for system dynamic studies," *IEEE Trans. Power Syst.*, vol. 7, no. 1, pp. 167–179, Feb. 1992.

Krishnakumar R. Vasudevan (Graduate Student Member, IEEE) received the B.E degree in electrical and electronics engineering and the M.E degree in power engineering and management from Anna University, Chennai, India, in 2016 and 2018, respectively. He is currently working toward the Ph.D. degree in electrical power engineering with the Department of Electrical Power Engineering, Universiti Tenaga Nasional (UNITEN), Kajang, Malaysia.

Since 2019, he has been a Research Engineer with the Institute of Power Engineering, UNITEN. His research interests include power systems, energy storage systems, pumped hydro storage, microgrid control and renewable energy.

Mr. Vasudevan was the recipient of Gold Medal and Silver Medal in his M.E and B.E degrees, respectively.

Vigna K. Ramachandaramurthy (Senior Member, IEEE) received the bachelor's degree (Hons.) in electrical and electronics engineering and the Ph.D. degree in electrical engineering from the University of Manchester Institute of Science and Technology, Manchester, U.K., in 1998 and 2001, respectively.

He then joined the Malaysian electrical utility, Tenaga Nasional Berhad, in 2002, as an Electrical Engineer. In 2005, he moved to Universiti Tenaga Nasional, Kajang, Malaysia, where he is currently a Professor with the Institute of Power Engineering. He is also a Chartered Engineer registered with the Engineering Council of U.K., and a Professional Engineer registered with the Board of Engineers Malaysia. He is also the Principal Consultant for Malaysia's biggest electrical utility, Tenaga Nasional Berhad. He has completed more than 250 projects in renewable energy. He has also developed several technical guidelines for interconnection of distributed generation and solar PV in Malaysia. His research interests include power systems, renewable energy, energy storage, power quality, electric vehicle, and rural electrification.

Dr. Ramachandaramurthy is also in the Editorial Board/Associate Editor of *IET Smart Grid*, *IET Renewable Power Generation*, IEEE SMART GRID, and IEEE ACCESS.

Gomathi Venugopal received the B.E degree in electrical and electronics engineering from Madras University, Chennai, India in 2002, and the M.E and Ph.D. degrees in power systems from Anna University, Chennai, India, in 2004 and 2011, respectively.

She is currently an Associate Professor with the Faculty of Electrical Engineering, Anna University, Chennai, India. Her research interests include smart grid, power system and cloud computing.

Josep M. Guerrero (Fellow, IEEE) received the B.Sc. degree in telecommunications engineering, the M.Sc. degree in electronics engineering, and the Ph.D. degree in power electronics from the Polytechnic University of Catalonia, Barcelona, Spain, in 1997, 2000, and 2003, respectively.

Since 2011, he has been a Full Professor with the Department of Energy Technology, Aalborg University, Aalborg, Denmark. He has also been the Chair Professor of Shandong University, since 2014, a Distinguished Guest Professor with Hunan University, since 2015, a Visiting Professor Fellow with Aston University, U.K., and a Guest Professor with the Nanjing University of Posts and Telecommunications, since 2016. In 2019, he became a Villum Investigator by the Villum Fonden, which supports the Center for Research on Microgrids, Aalborg University, where he is the Founder and the Director. His research interests are oriented to different microgrid aspects, including power electronics, distributed energy-storage systems, hierarchical and cooperative control, energy management systems, smart metering.

Dr. Guerrero was the recipient of Best Paper Award of the IEEE TRANSACTIONS ON ENERGY CONVERSION, from 2014 to 2015, the Best Paper Prize of IEEE-PES, in 2015, and the Best Paper Award of the *Journal of Power Electronics*, in 2016. During six consecutive years, from 2014 to 2019, he was awarded by the Clarivate Analytics (former Thomson Reuters) as a Highly Cited Researcher. In 2015, he was elevated as the IEEE Fellow for his contributions on distributed power systems and microgrids. He is an Associate Editor of several IEEE transactions.

Janaka B. Ekanayake (Fellow, IEEE) was born in Matale, Sri Lanka, in October 1964. He received the B.Sc. degree in electrical engineering from the University of Peradeniya, Galaha, Sri Lanka, in 1990, and the Ph.D. degree from the University of Manchester Institute of Science and Technology, Manchester, U.K. in 1995.

He is currently the Chair Professor of electrical and electronic engineering at the University of Peradeniya, Galaha,Sri Lanka. He is also a Visiting Professor with Cardiff University, Cardiff, U.K., and Universiti Tenaga Nasional, Kajang, Malaysia. He has authored or coauthored more than 75 articles in refereed journals and has also coauthored six books. His research interests include renewable energy generation and its integration and smart grid applications.

Dr. Ekanayake is also a Fellow of IET.

Sieh Kiong Tiong (Member, IEEE) received the B.Eng. (Hons.), M.Sc., and Ph.D. degrees in electrical, electronic and system engineering from the National University of Malaysia, Bangi, Malaysia, in 1997, 2000, and 2006, respectively.

He is currently a Professor with the College of Engineering and he is also the Director of the Institute of Sustainable Energy, Universiti Tenaga Nasional. He is a Professional Engineer registered with the Board of Engineers Malaysia. His research interests include renewable energy, artificial intelligence, data analytics, microcontroller systems, and communication systems.

Authorized licensed use limited to: Aalborg Universitetsbibliotek. Downloaded on February 18,2021 at 13:48:56 UTC from IEEE Xplore. Restrictions apply.